Mapping Crossing Myofiber Populations with Diffusion Spectrum Imaging in Simulated and Microfabricated Model Tissues

by

Jason Liang

SUBMITTED TO THE DEPARTMENT OF MECHANICAL ENGINEERING IN PARTIAL FULFILLMENT OF THE REQUIREMENTS FOR THE DEGREE OF

BACHELOR OF SCIENCE, MECHANICAL ENGINEERING
AT THE
MASSACHUSETTS INSTITUTE OF TECHNOLOGY

MAY 2005 [June 2005]

Signature of Author:

Department of Mechanical Engineering
May 9, 2004

Certified by:

Richard J. Gilbert, MD
Research Scientist, Department of Mechanical Engineering
Thesis Supervisor

Accepted by:

Ernest Cravalho PhD
Professor of Mechanical Engineering
Chairman, Undergraduate Thesis Committee

Mapping Crossing Myofiber Populations with Diffusion Spectrum Imaging in Simulated and Microfabricated Model Tissues

by

Jason Liang

Submitted to the Department of Mechanical Engineering
on May 9, 2004 in Partial Fulfillment of the
Requirements for the Degree of Bachelor of Science in
Mechanical Engineering

ABSTRACT

The ability to resolve complex myofiber populations is important for relating architectural structure with mechanical function in muscular tissues. To address this issue, we sought to validate the capacity of Diffusion Spectrum Imaging (DSI), an MRI method for assessing molecular diffusion in a confined geometry, to determine fiber alignment in tissues whose myofibers are aligned at varying orientations. By this method, molecular displacement in a tissue can be determined by Fourier transforming the echo intensity against gradient strength at fixed gradient pulse spacing. The displacement profiles are visualized by graphing 3D isocontour icons for each voxel, with the isocontour shape and size representing the magnitude and direction of the constituting fiber populations. Validation of DSI was accomplished with two sets of experiments: We simulated diffusive motion and a DSI experiment within the constraints of crossing fibers, and determined that DSI accurately depicts arbitrary angular relationships between crossing fibers. We also used DSI to accurately resolve the geometry of aligned channels in poly(dimethylsiloxane) (PDMS) microfluidic phantoms.

Thesis Supervisor: Richard J. Gilbert, MD
Title: Research Scientist in Mechanical Engineering

Table of Contents

List of Figures

1. Introduction

1.1 Tongue Mechanics

The tongue is a unique and versatile muscular organ, which, in the course of normal speech and swallowing, assumes a large array of shapes, positions, and degrees of mechanical stiffness (Figure 1). It is generally believed that the structural basis of this behavior is the tissue's extensively interwoven myoarchitecture, in which muscle fibers are characteristically aligned along multiple spatial axes. The determination of the tongue's complex myoarchitecture has long presented a challenge to students of structure-function relationships in muscular systems. The impact of this challenge is further seen when attempting to ascertain the structural basis of various lingual disorders.

Figure 1. Phases of swallowing depicted by MRI. In the oral stage of swallowing, the tongue configures the ingested bolus in the oral cavity (accommodation), and then propels the configured bolus from the oral cavity into the pharynx (propulsion).

From an anatomical perspective, the tongue consists of an overlapping three-dimensional network of skeletal muscle fibers and fiber bundles, involving both intrinsic fibers, i.e. those fibers possessing no direct connection to bony surfaces, and extrinsic fibers, i.e. those fibers possessing connections to bony surfaces.[1,2,3,4,5] The intrinsic musculature consists of a core region of orthogonally-aligned fibers, contained within a sheath-like tract of longitudinally oriented fibers. The intrinsic fibers are delicately merged with extrinsic muscles that modify shape and position from a superior

(palatoglossus), posterior (styloglossus), and inferior direction (genioglossus and hyoglossus). The fact that the intrinsic and extrinsic fibers appear to merge structurally along several geometric planes opens to question the classical anatomical distinction between "intrinsic" and "extrinsic" fibers, and suggests that the lingual myoarchitecture may more appropriately be considered as a continuum of variably oriented fibers. The demonstration of continuous properties in the setting of biological tissues requires a method for determining muscle fiber alignment along multiple planes and spatial scales in intact structures.

From a mechanical perspective, the tongue is generally considered to be a form of muscular hydrostat,[6,7,8,9,10,11] an organ whose musculature both creates motion and supplies skeletal support for that motion. As such, it capitalizes on its high water content, and hence incompressibility, to modify its form, without change in volume. By definition, all hydrostats in nature possess fibers parallel and perpendicular to the organ's long axis, but differ regarding the relative position and geometry of the perpendicular fibers. For example, muscular hydrostats that principally perform bending motions tend to have longitudinal fibers farther away from the longitudinal axis. An example of this phenomenon is the snake, which typically flicks its chemoreceptor-laden organ to sense its prey. The fibers of the elephant trunk, on the other hand (Figure 2), are organized in a

Figure 2. The elephant trunk as an example of a muscular hydrostat. A muscular hydrostat is an organ composed almost entirely of muscle, whose musculature produces deformation and the structural support for that deformation. These organs are incompressible, hence tissue volume is conserved. Note that in this instance, the fibers are organized in a spiral orientation relative to the central longitudinal axis, thereby maximizing the capability of the elephant to perform twisting patterns of deformation.

spiral fashion about the central longitudinal axis, thereby maximizing the ability of the organ to perform the twisting deformations needed for grasping arboreal vegetation. The tentacle of the squid, which is most structurally similar to the mammalian tongue, has a core region of transverse fibers surrounded by a longitudinal sheath.

While there is much diversity in the animal kingdom regarding the manner in which the tongue manifests its hydrostatic properties, the pervasive morphological construct is the presence of orthogonally aligned set of muscle fibers. The mammalian tongue is, in fact, a unique form of muscular hydrostat, inasmuch as it embodies both intrinsic and extrinsic fibers. In this manner, deformations resulting from contractions of the intrinsic components of the hydrostat may be augmented and modified by extrinsic elements that tether to the surrounding skeletal structure. Synergistic contractions of extrinsic and intrinsic muscles of the tongue, anatomically indistinct at the point of their insertion in the body of the tongue, may thus contribute to hydrostatic deformations. Given the complexity of the tongue's myoarchitecture, these motions may produce a near infinite number of combinations, involving hydrostatic elongation (with associated tissue stiffening) and displacement, secondary to the activation of intrinsic and directionally specific extrinsic fibers.

Despite the large impact of lingual disorders on the health and well-being of patients with neuromuscular disease, there is remarkably little known of the underlying mechanical mechanism for these disorders. An approach is therefore necessary which helps determine structure of living tissue, both healthy and infected, providing a biomechanical basis for understanding lingual disease. Similarly, the biomechanical muscular principals of the tongue can also be applied to other muscular systems in the

human body. Since the understanding of how complex myoarchitectural patterns translate into strain is generic for all muscular systems in the body, this approach should have broad applicability for the diagnosis, stratification, and monitoring of treatment for numerous cardiac and skeletal muscle diseases.

1.2 NMR Imaging Methods

Conventional tissue imaging methods, such as ultrasound, CT Scanning, and most forms of MRI, do have the ability to determine details of internal structure. However, Nuclear Magnetic Resonance Imaging (NMR) of proton diffusivity has the capacity to infer fiber architecture by determining fiber direction.[12,13,14,15] This is done by tracking molecular diffusion along muscle fibers. Diffusion weighted imaging uses the concept of Q-space, a quantitative way to conceptualize how such diffusion data might be used to study complex microscopic structures, and specifically relates diffusion-based imaging points to spatial dimensions. [16,17,18, 19] Q-space imaging uses the Fourier transform relationship to derive the probability density function (PDF) for spin displacement from the attenuation of the diffusion signal, with the assumption that barriers, biological or otherwise, create directionally specific dissimilarities in molecular diffusion.

A simplified type of diffusion-weighted imaging termed diffusion tensor imaging (DTI), has been employed by Dr. Gilbert's laboratory to determine fiber orientation in excised sheep and cow tongues ex vivo[20,21,22] as well as other tissues, including the heart[23,24,25,26,27,28] and brain.[29,30,31] DTI is generally able to resolve data to determine a principal fiber direction (principal eigenvector) and thus creates a 3-D anatomical map of a given tissue (Figure 3 and 4). While DTI is most accurate in analyzing fiber direction

for regions of homogeneous myofiber alignment (all fibers are predominantly parallel at the scale of the individual voxel), it is limited for determining fiber alignment in the setting of more complex fiber patterns, such fiber crossing or divergence, and other non-parallel fiber alignments. DTI is further limited in that it assumes that intravoxel diffusion follows a Gaussian model and that fluid exchange across restrictive membranes is relatively slow, conditions unlikely to occur in biological tissue. As a result, a more general and robust diffusion method is needed, which is capable of tracking molecular diffusion in all directions, and thus more accurately quantify the orientation of complex fiber populations in biological tissues and other similar structures.

A variation on q-space imaging, termed diffusion spectrum imaging (DSI) [32, 33] has been employed in Dr. Gilbert's laboratory to study whole tissue fiber architecture. DSI takes hundreds of diffusion weighted MR images each with a different diffusion weighting gradient value and angularity. This procedure determines a complete 3D spin displacement function for each voxel. Thus, DSI allows for the quantification of fiber direction in regions where fibers overlap or merge, and provides a method for resolving more the complex myoarchitectural patterns typical of many muscular structures.

DSI has been shown to accurately resolve crossing anoxal fibers in phantoms under such conditions where gradient duration is infinite with respect to diffusion time, and in rat optic tracts under conditions where gradient duration is finite[34]. We attempt here, to validate DSI and its ability to correctly resolve heterogeneously aligned fibers using microcapillary phantoms created to simulate a muscular tissue environment in which fibers are aligned in parallel and non-parallel orientations.

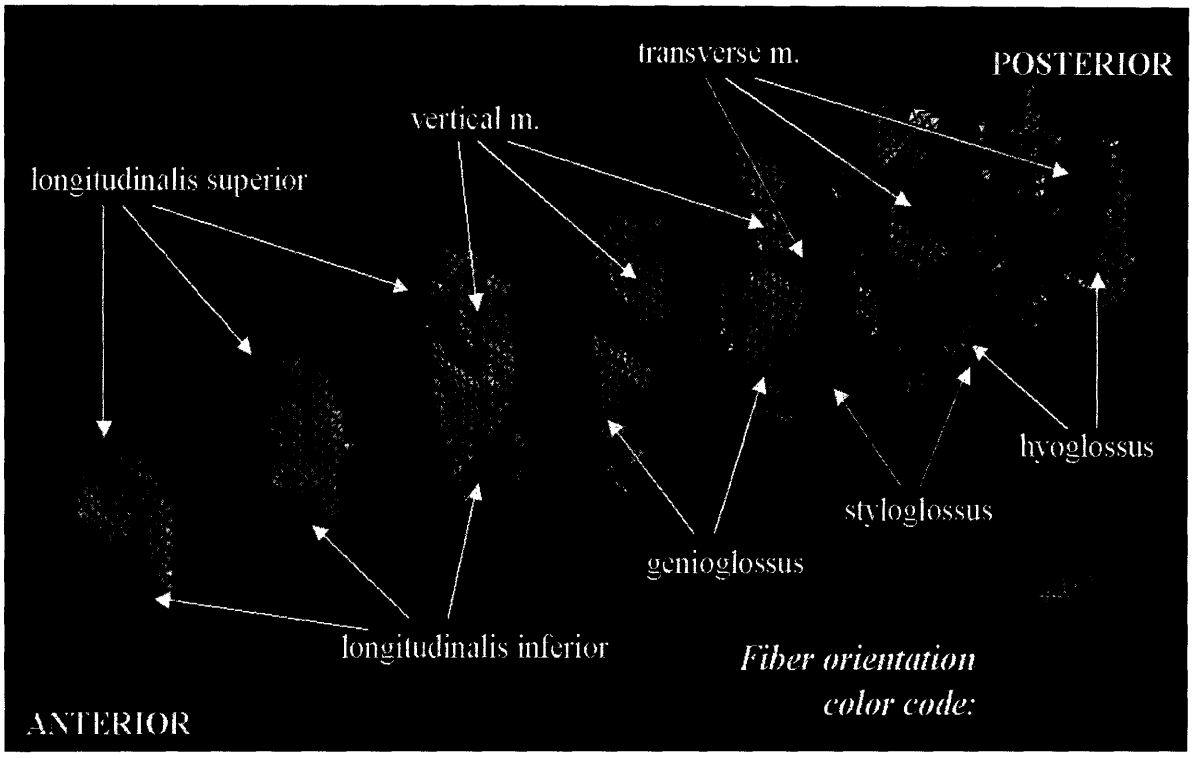

Figure 3. DTI of excised cow tongue Data displayed for each voxel in terms of the principal fiber direction, or the principal eigenvector, which points in the direction of the predominant fiber population. 3D fiber orientation color coded as shown. The location of specific muscle groups are shown for anatomic reference.

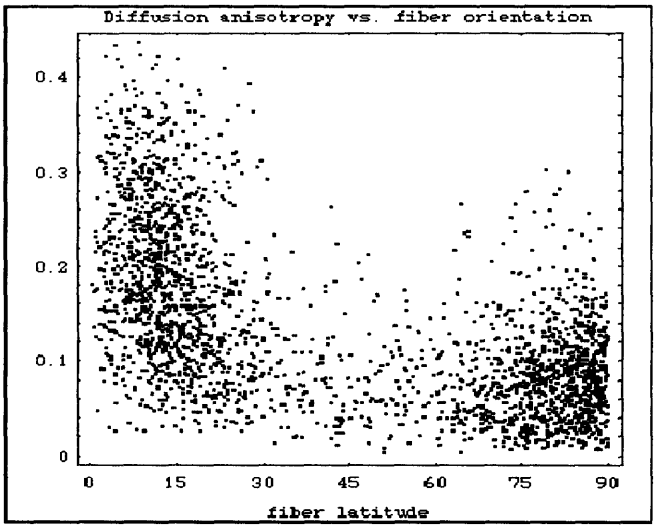

Figure 4. Diffusion anisotropy: cow tongue (axial) Anisotropy depicted as a function of fiber angle relative to longitudinal axis. Diffusion anisotropy ($\lambda 1/\lambda 2$) is high if the voxel contains a single unidirectional set of fibers and low if the voxel contains fiber populations in multiple directions. Fibers parallel to longitudinal axis (sheath) display high anisotropy, whereas fibers perpendicular to longitudinal axis (core) display low anisotropy.

2. Methods

2.1 Research approach

In order to further validate DSI for purposes for resolving the crossing fiber populations of the tongue, and potentially other tissues, we have designed two types of experiments: 1) In the first, we have simulated crossing fiber populations using a graphical computer program, then assessed the ability of a simulated DSI magnetic resonance imaging experiment to resolved these crossing fibers. 2) In the second, we have fabricated using soft lithography a set of microfluidic capillaries to mimic muscle fibers, and assessed the ability of DSI to resolve these "myofiber" populations, when aligned in parallel and crossing patterns.

2.2 Theoretical Basis for Diffusion Spectrum Imaging

In general, diffusion attenuates the MR signal because the probability of finding a proton that has spread from its starting point increases with diffusion. Physical boundaries, such as cell membrane or cytoskeletal elements, limit diffusion in a given orientation and thus narrow the probability spread. Since muscle fibers are elongated cells with a semi-permeable sarcolemma, water should diffuse more readily along the fiber axis, than perpendicular to it, thus yielding anisotropy at the scale of the individual myofiber. The technical challenge of magnetic resonance imaging is to determine the orientation of large numbers of fibers and fiber populations when a defined segment of tissue.

The concept of Q-space was proposed as a way to conceptualize how such diffusion data might be used to study complex microscopic structures, and specifically

relates diffusion-based imaging points to spatial dimensions.[35,36,37,38] Q-space imaging uses the Fourier transform relationship to derive the probability density function (PDF) for spin displacement from the motion-dependent attenuation of the diffusion signal, with the assumption that biological barriers create directionally specific dissimilarities in molecular diffusion. Diffusion Spectrum Imaging is a subset of q-space imaging methods, and specifically portrays the behavior of a construct termed the average diffusion propagator ($\bar{P}_s$) in an enclosed space. The advantage of the diffusion propagator is that it does not follow any geometric model. It also does not assume any specific diffusive process. This is in contrast to other forms of diffusion imaging such as DTI which assumes diffusion under Gaussian conditions i.e. an anisotropic medium with no boundaries. Furthermore, DTI only shows one fiber direction per voxel. It is therefore less accurate in representing human tissue where fibers in a given voxel may cross or diverge. DSI represents a subset of q-space imaging, defined as a method for representing the 3D spin displacement probability density function for each voxel. In practice, many diffusion weighted MRI images are taken, each with different diffusion weighting gradient value. Diffusion weighting gradient values corresponds to equally spaced points in a sphere, ranging from maximum to minimum strength in the X, Y, and Z directions. Data points contained in each voxel is equal to specific q-value (gradient strength) corresponding to image from which it was taken.

A diffusion sensitive pulse sequence in its most basic form is comprised of a bipolar gradient pulse sequence designed in such a way that spins of molecules that do not move are unaffected by the pulse where molecules that do move change phase. The phase of a spin is given by equation 2

$$\varphi_j = \gamma \int \mathbf{g}^*(t') \cdot \mathbf{r}_j(t') dt' \tag{1}$$

where **g** is defined as the effective diffusion-weighting gradient. The conventional pulsed-gradient spin-echo (PGSE) sequence consists of the standard bipolar gradient pulse sequence (g and -g) of width δ and each pulse is separated by some time Δ, where δ is infinitesimally small with respect to Δ. The NMR signal acquired is the sum of all of the spin phases acquired

$$M(t) = \sum_j \exp(i\varphi_j) . \tag{2}$$

Now, if the wavevector **q** is defined as $\mathbf{q} = \gamma\delta\mathbf{g}$ we can say that

$$M(t) = \sum \exp(i\mathbf{q} \cdot \mathbf{R}) \tag{3}$$

The sum of all the phases is merely the probability densities integrated over all possible starting distances **r** and ending distances **R.**

$$M(\mathbf{q},t) = \iint \rho(\mathbf{r}) P_S(\mathbf{R} \mid \mathbf{r}, t) \exp(i\mathbf{q} \cdot \mathbf{R}) d\mathbf{r} d\mathbf{R} . \tag{4}$$

then, if $t > \delta + \Delta$, phase no longer changes. Then, since δ is infinitesimal, M no longer becomes a function of t. The result is

$$M(\mathbf{q},\Delta) = \int \bar{P}_S(\mathbf{R},\Delta) \exp(i\mathbf{q} \cdot \mathbf{R}) d\mathbf{R} . \tag{5}$$

Where $\bar{P}_S$ is the average diffusion propagator such that

$$\bar{P}_S(\mathbf{R},t) = \int \rho(\mathbf{r}) P_S(\mathbf{R} \mid \mathbf{r}) d\mathbf{r} \tag{6}$$

The average diffusion propagator is defined as the sum of the probability density functions (P_S) multiplied by $\rho(\mathbf{r})$, the proton density distribution. **R** is the distance water molecules move away from the starting point (**r**) due to diffusive motion. We are able to

consider the use of a probability density function since diffusion is regarded here as a random process. Equation (6) is also the Fourier transform of $\overline{P_s}$ in q-space

$$\overline{P_s}(\mathbf{R},\Delta) = \mathrm{F}^{-1}\left[M(\mathbf{q},\Delta)\right] \tag{7}$$

In order to achieve practical q-space imaging, DSI modifies the pulse sequence to include non-infinite pulse width[39]. When the pulse width δ is finite, the equations become more complex. If Gaussian conditions are assumed during constant gradient application (i.e. during δ), then the diffusion time in the above equations is replaced with an effective diffusion time[40]:

$$\Delta_e = \Delta - \delta/3 \tag{8}$$

If Gaussian diffusion cannot be assumed during δ, as is most likely to be case in the biological realm, then the center-of-mass (COM) diffusion propagator is the relevant representation. This formalism accounts for the fact that non-random molecular displacements occur during the duration of δ.

2.3 Finite Element Modeling

To validate DSI, we performed a simulation with finite element analysis of water diffusion, whereby DSI imaging and data analysis were performed for an artificial set of crossing fibers. The data was represented as the probability density function for a diffusion signal per voxel owing to the fact that Q-space has a Fourier transform relationship to the probability density function in the voxel. Since analytic solutions involving complex structures and boundary conditions are not feasible, we performed finite element simulations to assess the behavior of these diffusion propagators. The spatial scaling is in the order of normal skeletal muscle fibers, i.e. 20μm width and

200μm length. We provide below finite element simulations of the behavior of a diffusion propagator for a simple set of two-dimensional crossing fibers with communicating water. The general finite element simulation was constructed and solved using MATLAB (The MathWorks Inc, Natick, MA) using the following diffusion equation, which was determined for each element:

$$\frac{\partial P_S(\mathbf{R},\mathbf{r})}{\partial t} = D\nabla^2 P_S(\mathbf{R},\mathbf{r}), \tag{9}$$

with D as a constant isotropic diffusion term and $P_S(\mathbf{R},\mathbf{r})$ is the diffusion propagator (i.e. the probability distribution of spins having diffused a distance $\mathbf{R}$ given the initial condition $\mathbf{r}$).

2.4 Design of Microfluidic "Phantoms"

The phantoms were created using soft lithography, a relatively inexpensive and reproducible method for carrying out micro- and nano-fabrication[41] (Figure 5). During soft lithography, a master slide is created with patterned relief structures. These structures create channels ranging from ~30 nm to ~100 μm. A polymer is then poured over this slide cured, and then peeled off.

The master for these phantoms was created using a negative photoresist. During this process, photoresist is poured over a 3.5in Si wafer (Silicon Quest, Santa Clara, CA). The unit is spun to create a thin, even film or a desired height and then baked until hard. Lithography masks (Mika color, CA) were designed and printed at 3550 dpi. They were placed over the hardened photoresist and then entire unit is exposed to UV light. Polymethylacetate (PMA) (Microchem, Newton, MA) was then used to remove all the unexposed photoresist. The remaining photoresist is the relief on the master slide.

Finally, a polymer is poured over the master and baked. The hardened polymer is the microfluidic structure.

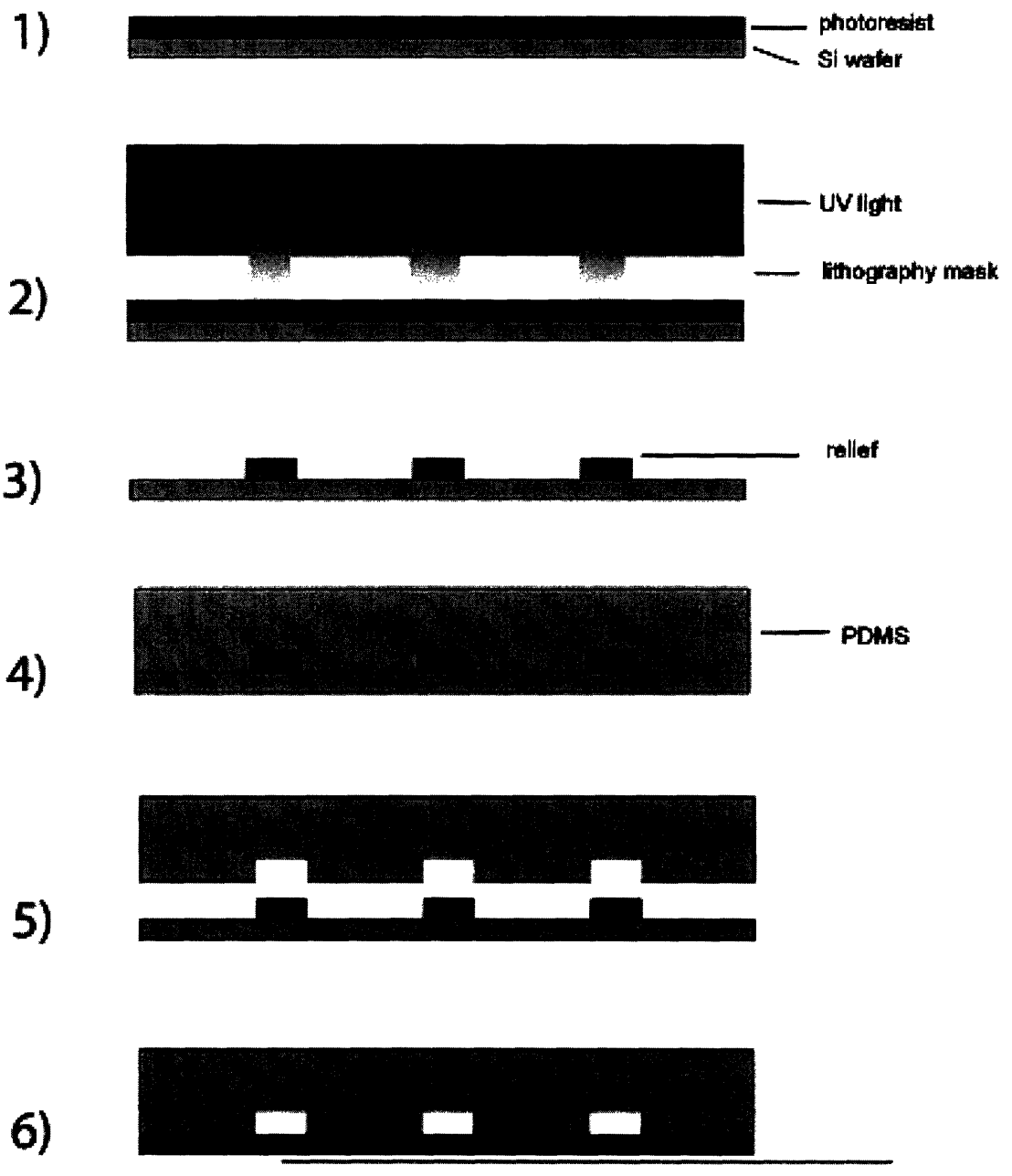

Figure 5. Fabrication of microfluidic phantoms. We demonstrate the stages involved in the fabrication of microfluidic chips. 1) Generation of master using negative photoresist resulting in lithography masks. 2) Masks placed over hardened photoresist, which is exposed to UV light to generate 3) a master slide relief. 4) Polymer is poured over master slide and baked, and 5) the master slide relief removed, to create 6) the microfluidic construct.

For this set of phantoms, the master slide reliefs were 100μm wide, 100μm tall, and 150μm apart. The master was coated with poly(dimethylsiloxane) (PDMS) (Robert McKeown, Cambridge, MA). PDMS was chosen because of its numerous properties that make it very useful for soft lithography[42]. PDMS comes in a two part kit: a liquid monomer and a curing or crosslinking agent. The two parts are mixed together at a ratio of 20:1 (monomer:crosslinking agent) and then poured onto the master and spun to create a thin layer. The master/polymer complex is baked to slightly harden the polymer. The process is repeated with another master slide, except the PDMS is poured on heavily to create a thick film. The thick polymer is cut from the master and then placed on top of the thin polymer layer. Finally, the complex is baked again. The final product is a bi-layer phantom. (Figure 6)

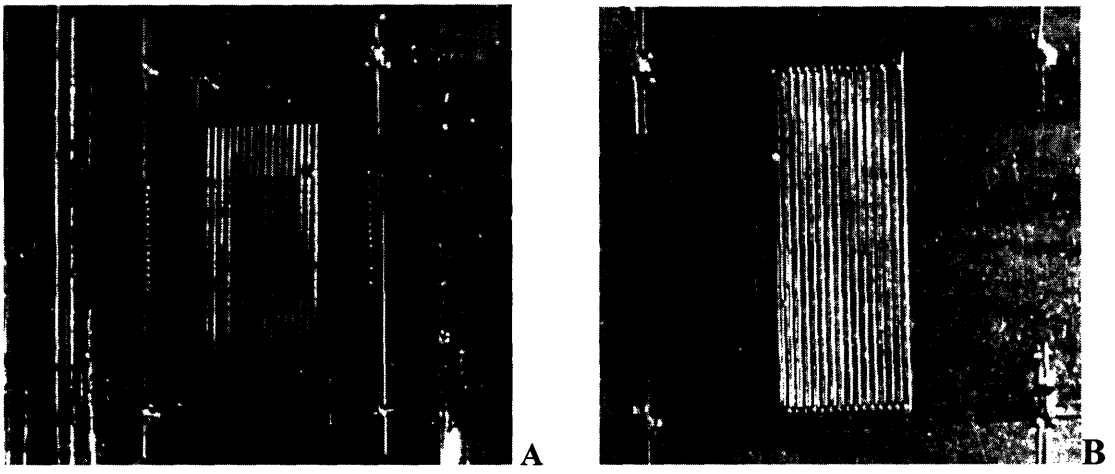

Figure 6. Microfluidic phantoms. Shown are actual photographs of A) microfluidic structures with orthogonally aligned channels created using soft lithography, and B) microfluidic structures created with parallel channels created with soft lithography.

2.5 Magnetic Resonance Protocol

Diffusion weighted imaging was applied to two groups of phantoms and several scans were run with each group. 1 group had phantoms with parallel channels, while the other

had orthogonally aligned channels. The channels of these phantoms were filled with water and contained water during the duration of the scan. For these scans, a diffusion sensitive stimulated-echo pulse sequence was used. Diffusion time was 500ms while pulse width was .5ms for parallel and crossing channels, and 10ms for crossing channels. The gradient strength g was 330mT/m for parallel channels, and 330mT/m as well as 16.5mT/m for crossing channels.

3. Results

3.1 Finite Element Analysis

We performed finite element analysis to asses the behavior of the diffusion propagator on structures simulating 2-D crossing fiber populations with communicating intrafiber space (Figure 7). The simulation was repeated for each mesh points (starting values of **r**). The average propagator was the sum of all of the probability density functions from each mesh point within the structure, assuming constant molecular density. The computed average diffusion propagator is shown in Figure 7B at t = 500 ms. The value of the average diffusion propagator is greatest in the center (as indicated by the red color) due to the fact that molecules have the greatest probability of remaining around their origin and that molecules are inherently limited in the number of directions that they can diffuse from their origin. Also shown are spikes protruding from the center. These represent the known fiber directions. These spikes decrease in intensity quickly since larger diffusion distances become increasingly more improbable farther away from the center. The resulting ordientational distribution function (ODF) was calculated with equation and provided coloring and radius values corresponding to its values (Figure 7C). Figure 7D shows the extension of MATLAB simulation to include a DSI pulse sequence and the Fourier transform reconstruction. The spins acquire spatially dependent phase shifts from magnetic field gradients as specified by equation 1. The gradients applied correspond to a keyhole Cartesian grid of **q** vectors. For each **q** vector, a phase shift acquired for each mesh point delta-function initial-condition is calculated by using the pulsed gradient applied at several different discrete simulation time steps, and summed

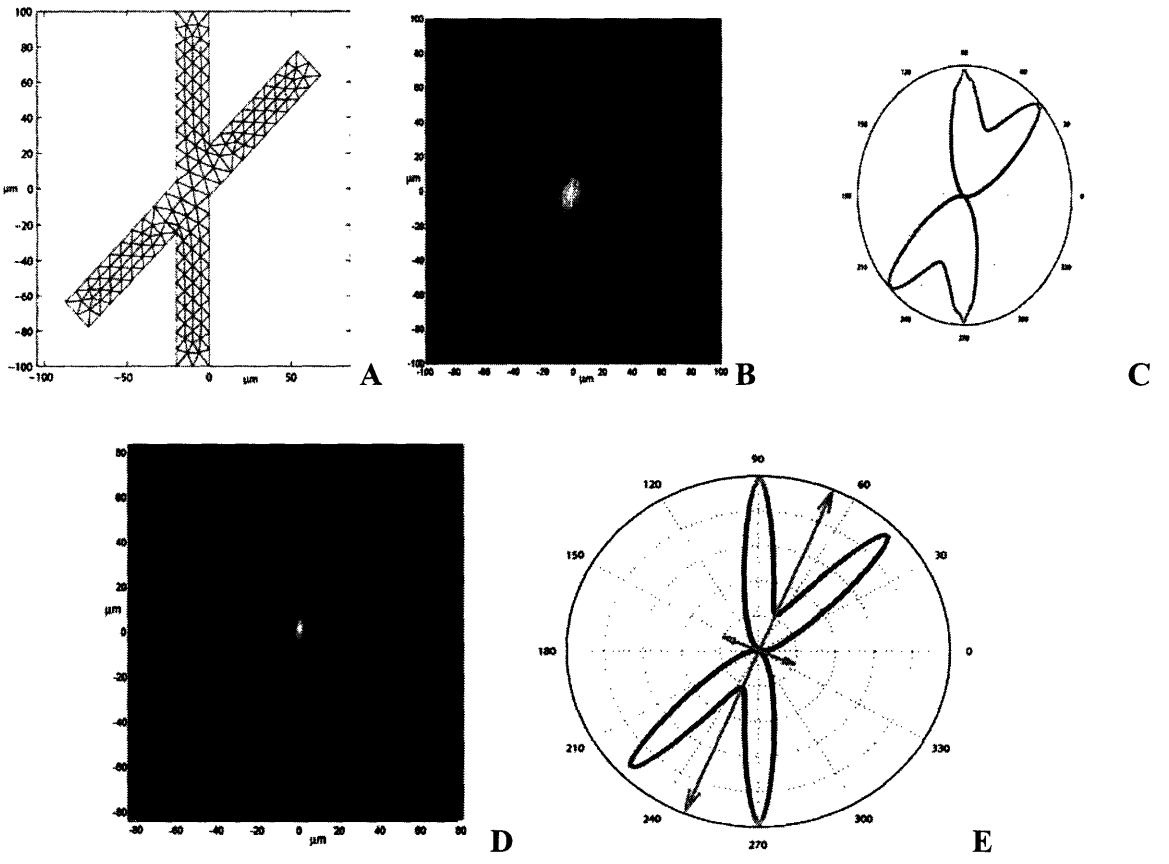

Figure 7. Finite element simulation for diffusion imaging of model crossing fibers. Finite element simulations were obtained in order to portray the behavior of a diffusion propagator for a simple set of two-dimensional crossing fibers with communicating water, employing water diffusion at $t = 500$ ms and isotropic water diffusion coefficient $D = 2.5 \times 10^3$ μm^2/s. A) Automatically generated finite element mesh with 189 points depicting realistic geometry of size and angular relationship for crossing skeletal muscle fibers. B) Image depicting the average diffusion propagator $\overline{P_s}$ computed from the simulation. C) Radially weighted orientational distribution function (ODF) computed from the image in part (d). D) Simulation of an actual DSI experiments employing the crossing fiber model shown in (A). A finite pulse-width PGSE sequence was simulated with $\delta = 350$ ms, $\Delta = 600$ ms, and a 10 mT/m maximum gradient strength. The resulting diffusion propagator obtained from the simulation is shown. This propagator has is physically interpretable as the center of mass (COM) propagator. E) Radially weighted ODF superimposed on the eigenvectors calculated from the simulation data using a DTI approach. The maximum DTI eigenvector is limited to bisecting the two simulated fibers.

across time. The values of the gradients applied are positive **q** for $0 < t < \delta$, zero for $\delta < t < \Delta$, and negative **q** for $\Delta < t < \Delta + \delta$. The resulting phases for all mesh point simulations are then summed together with equation 0, resulting in the signal for that

value of **q**. The signal values obtained fill a 2D array indexed by **q**. The 2D Fourier transform is calculated resulting in the COM average diffusion propagator shown Figure 1D. This propagator has similar features to the average diffusion propagator except that it possesses beneficial sharpening of its peaks. The ODF is shown with a superimposed DTI solution for this simulation (Figure 7E), confirming the inability of DTI to resolve the angularity of crossing fibers.

3.2 Microfluidic Structures

Figure 8 shows the phantoms arranged in parallel channel populations obtained by DSI and viewed as a set of ODFs and color coded relative to direction. In this image, each color represents a different principal direction. Red indicates the horizontal direction, green indicates the vertical direction, and blue indicates the direction in the plane of the page. We show here how DSI can accurately resolve regions of homogeneously aligned populations. This is indicated by the dominant red directional component. Correctly, the voxels outside the region of the phantom show no evidence of sustained directionality. We further attempted to resolve the fibers present in orthogonally aligned channel populations in microfluidic phantoms. We hypothesized that the orthogonal relationship existing between the microfluidic capillaries would be reflected in ODFs, whose shape explicitly was consistent with such orthogonality. However, we encountered a problem with the MR pulse sequence, resulting in the fact that symetrical images did not appear identical. As a result, our ODFs intended to validate the ability of DSI to show multiple overlapping fiber populations were inconclusive.

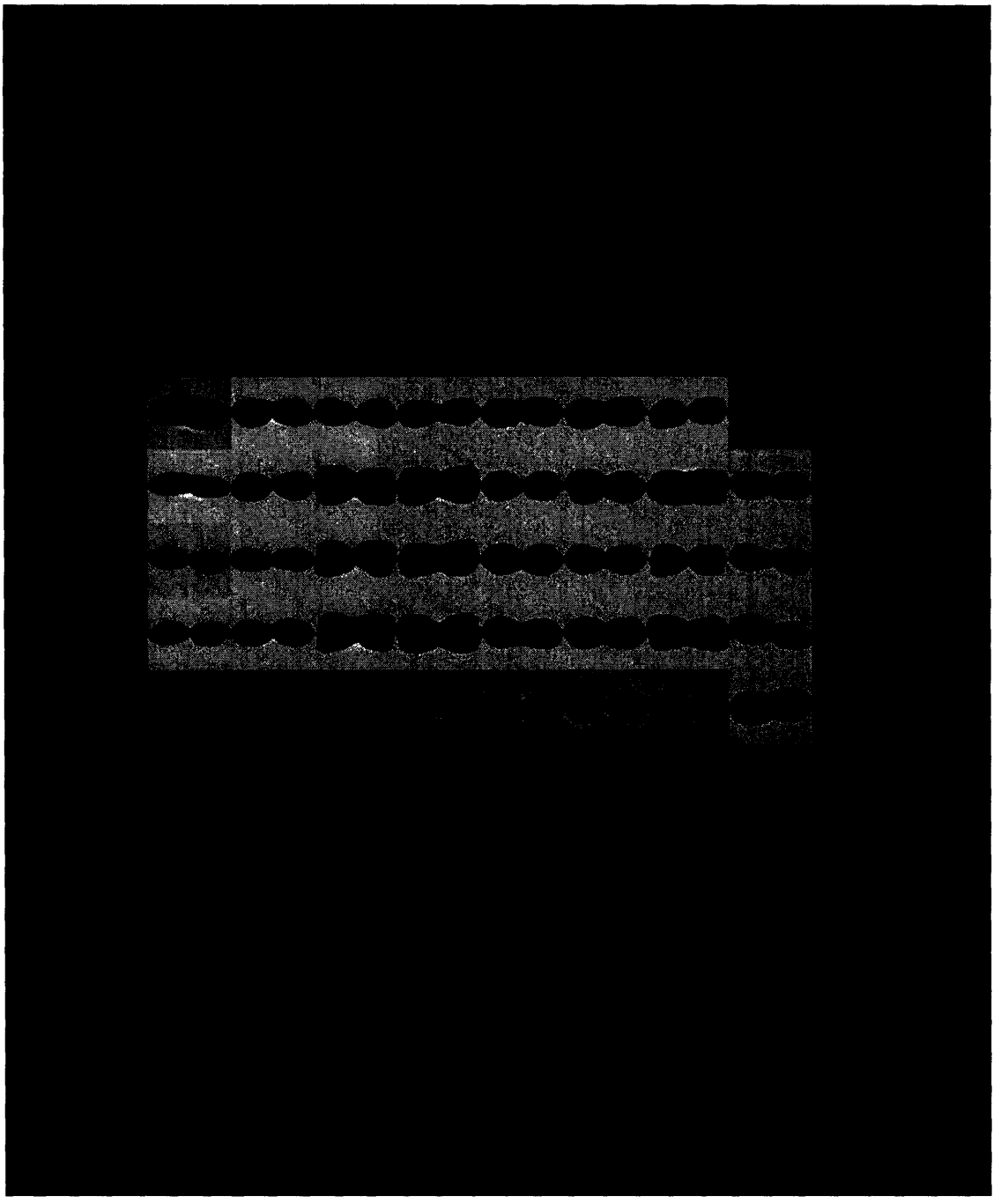

Figure 8. Orientational distribution functions for a DSI scan of microfluidic phantoms. The ODFs for a phantom arranged in parallel fibers. Channels exist in the rectangular set of voxels in light gray. The ODFs in these regions align with each other and show the unidirectional orientation of the channels.

4. Discussion

From a mechanical perspective, the tongue is generally considered to be a muscular hydrostat[43, 44, 45, 46, 47, 48] an organ whose musculature both creates motion and supplies skeletal support for that motion. To do this, it utilizes its high water content, and hence incompressibility, to change its shape, without changing its volume. By definition, all hydrostats in nature possess fibers parallel and perpendicular to the organ's long axis, but differ in the position and geometry of the perpendicular fibers. While there is a lot of diversity in the animal kingdom regarding the way the tongue demonstrates its hydrostatic properties, the prevailing belief is the presence of orthogonally aligned set of muscle fibers. The mammalian tongue is, in fact, a unique form of muscular hydrostat, because it has both intrinsic and extrinsic fibers. Deformations resulting from contractions of the intrinsic fibers may be modified by extrinsic elements attached to the surrounding skeletal structure. Synergistic contractions of extrinsic and intrinsic muscles of the tongue may thus contribute to hydrostatic deformations. Given the complexity of the tongue's myoarchitecture, these motions may produce a near infinite number of combinations, involving hydrostatic elongation (with associated tissue stiffening) and displacement, as well as the activation of intrinsic and directionally specific extrinsic fibers.

To define the myoarchitecture of the tongue, we previously employed diffusion tensor imaging (DTI) as a method to examine its uncrossed and crossing fiber regions[49, 50, 51]. In so doing, we were able to resolve the muscles of the tongue based on the principal direction of fibers and the local angular dispersion of these fibers within the imaged sample. By this method, principal fiber orientation corresponds to the leading eigenvector

of the diffusion tensor, whereas the second eigenvector identifies the orientation of maximum fiber angle dispersion. Through the measure of diffusion anisotropy, a scalar whose magnitude reflects the degree of fiber alignment per voxel, we observed a clear discrepancy in the anterior tongue between the core fibers, comprised of the orthogonally oriented vertical and transverse muscles, (low anisotropy, uniaxial structures), and the sheath fibers comprised of the longitudinal muscles, (high anisotropy, multiaxial structures). These observations supported the concept of hydrostatic expansion, by which simultaneous contractions of the vertical and horizontal core muscles cause the tongue (via conservation of volume) to protrude in the anterior-posterior axis at right angles to these fibers. However, relating 3D-resolved myoarchitecture of the intrinsic musculature at macroscopic scales (determined by MRI) with its microscopic anatomy (determined by multiphoton microscopy), we observed a fundamental weakness of DTI in quantifying the geometry of fiber populations with a high degree of overlap or convergence. In these cases, the principal eigenvector of the diffusion tensor tended to alternate among several orientations, making the determination of specific fiber orientations ambiguous. Explicit measures of fiber orientation using a single second-order tensor yields a result intermediate between the actual fiber orientations.

Comparatively, DSI offers several advantages for morphologically complex regions of muscular tissue. DSI, which is based on an NMR depiction of the average diffusion propagator formalism, derives an average probability density function without the requirement of a Gaussian model to describe diffusive behavior. The average diffusion propagator is the sum of the set of molecular displacements occurring as a function of molecular motion. Each probability density function indicates the average

probability of a spin undergoing a given displacement over a given diffusion time. The data obtained by a DSI experiment is based on the Fourier relationship between the average diffusion propogator and the diffusion signal for the spin echo obtained at various gradient strengths. The use of the inverse Fourier transform of the diffusion signal thus allows for the reconstruction of the average diffusion propagator for a given voxel, a formalism termed q-space imaging.[52] Q-space is simply a method of bookkeeping MRI image acquisitions to enable a complete diffusion propagator reconstruction. The MRI images taken are indexed by their q-space directional coordinates for use in the 3D Fourier transform reconstruction. By measuring the three dimensional diffusion function, DSI depicts complex fiber relationships as the multimodal behavior of the diffusion propogator within a macroscopically resolved voxel of tissue.

A post-processing step for the diffusion propogator is necessary to make visualization possible in a two dimensional image. This step transforms the propagator into an orientational distribution function (ODF) with spatially dependent coloring and three dimensional shaded polygon shapes. The ODF is a transformation of the PDF from Cartesian to spherical coordinates for maximizing diffusion contrast, i.e. distinguishing different diffusion modes. The transformation selected for this dataset was a conversion to spherical coordinates, followed by radial integration weighted by the diffusion distance. This produced well defined peaks in the ODF corresponding to maximum diffusion directions. Weighting by the diffusion distance physically relates to attributing more value to spins which were able to diffuse over longer distances. This weighting is

beneficial also by removing the large isotropic signal at the center of the propagator where there is little spatially dependent contrast.

The computer simulations of q-space imaging and DSI show how DSI can offer advantages for resolving morphologically complex regions of muscular tissue. Here, the methods for creating a 2-d average diffusion propagator were used. The resulting average diffusion propagator correctly shows the probability distribution one would expect for such an object. Since the simulation was done explicitly in 2 dimensions only, the ODF appears differently than it would in 3 dimensions.

The relevance of a finite pulse width is also shown through the computer simulations. Figures 3 show that not only DSI can accurately resolve complex fiber populations with a finite pulse width, but it can actually increase the population differentiation. While the use of the COM propagator is more mathematically complex, we show here how it can more accurately resolve crossing fiber populations. Furthermore, the use of a finite pulse width is necessary to make the procedure clinically applicable since infinite pulse widths are not safe for clinical use.

Our first scan using q-space imaging of homogeneously aligned channels yielded resolved parallel channel orientation. This was consistent with our predictions. We then proceeded to scan phantoms with orthogonally oriented channels. After noticing a number of problems, we began to question the quality of the pulse sequence. Upon further analysis, we noticed that symmetrical images were not the same. While symmetric images have opposite gradients, they have equal magnitudes. Since the data collection is not direction specific, these images should look nearly identical. However,

since they clearly did not match, it became clear that there was a problem with our pulse sequence.

Had the pulse sequence been correctly in tact, we should have accurately resolved the orthogonal alignment of the microfluidic channels. The ODFs produced should be consistent with the direction of the channel direction, and accurately represented the angular relationship between the two sets of channels. However, due to the time constraints on this experiment, we were unable to correct the underlying problem with the pulse sequence and retry the experiment to correctly resolve crossing populations.

The next step would be to correct the problem with the pulse sequence and then perform a DSI experiment on crossing channel phantoms. After successfully resolving heterogeneous fiber populations, we would like to perform DSI experiments on phantoms with narrower channels. The current phantoms utilize channels which are 100μm across. When we consider the dimensions of muscular fibers, 100μm is large in scale and therefore narrower channels would more accurately depict how DSI would perform in actual tissue. Smaller channels would also enable us to shorten the scan time for future experiments since the current phantoms prevent us from shortening the diffusion time. This is driven by the need for water molecules to sample boundaries in order for diffusion imaging to be successful. Smaller channels on the order of 10μm would allow us to decrease the diffusion time and shorten the length of our scans greatly. Unfortunately, narrower channels decrease the total amount of water per voxel resulting in a lower signal to noise ratio. Currently, the microfluidic fabrication process of soft lithography makes it extremely difficult to create structures with multiple layers of such narrow channels. Ideally, we would be able to fabricate microfluidic phantoms with the capacity to hold

enough water to produce a signal to noise ratio which allows us to accurately resolve diffusion across the channels. Along similar lines, we would like to be able to vary the diffusion time associated with DSI. Longer diffusion times result in longer scan times, while shorter diffusion times prevent water molecules from sampling boundaries. Furthermore, as time increases, strength of signal decreases. We hope to develop a method which allows us to optimize diffusion time for a given sample.

Ultimately, the goal is to extend q-space imaging into the realm of clinical imaging, while clearly desirable, will embody several technical challenges. As initially conceived, q-space imaging embodies the application of negligibly short pulses (compared to the interval between pulses, or diffusion time,) and rapid rise times. Under these circumstances, the displacement distribution of molecules within the diffusion space is a function of the net displacement of the intended molecules. This allows for the development of the concept of the PDF, which expresses the mean probability of a spin displacement over a given diffusion time. The Fourier relationship between echo magnitude and the PDF allows for the reconstruction of the PDF by applying the inverse Fourier transform of the diffusion MR signal with respect to the molecular displacement wave vector. The use of infinitely short and strong pulses is often associated with the induction of significant eddy currents, which interfere with the imaging gradients and cause image distortions. In addition, typical q-space acquisition sequences require a gradient strength which may exceed clinical safety standards based on the specific absorption of radiofrequency energy. By its use of finite length pulses, DSI may constitute a compromise method by which q space imaging of muscular tissues may be performed in vivo.

References

[1] Abd-El-Malek, S. 1939 Observations on the morphology of the human tongue. J. Anatomy, 73: 201-210.

[2] Barnwell Y.M. 1976. Human lingual musculature: An historical review. International J. of Oral Myology, 2: 31-34.

[3] Miyawaki, K. 1974. A study of the musculature of the human tongue. Annual Bulletin of the Research Institute of Logopedics and Phoniatrics - University of Tokyo 8, 23-50.

[4] Sonntag C.F. 1925. The comparative anatomy of the tongues of mammalia. XII. Summary, classification, and physiology. J. Zool. Proc.of the Zool Soc. London, 21: 701-762.

[5] Takemoto, H. 2001. Morphological analyses of the human tongue musculature for three-dimensional modeling. J. Speech, language, and Hearing Res., 44: 95-107.

[6] Smith K.K., Kier W.M. 1989. Trunks, tongues, and tentacles: moving with skeletons of muscle. American Scientist **77**, 29-35.

[7] Kier W.M., Smith K.K. 1985. Tongues, tentacles and trunks: The biomechanics and movement of muscular hydrostats. Zool. J. Linn. Soc., 83: 307-324

[8] Nishikawa K.C., Kier W.M., Smith K.K. 1999. Morphology and mechanics of tongue movement in the African pig-nosed Hemisus Marmoratum: A muscular hydrostatic model. J. Exp Biol., 202: 771-780.

[9] Napadow V.J., Chen Q., Wedeen V.J., Gilbert R.J. 1999. Intramural mechanics of the human tongue in association with physiological deformations. J. Biomechanics, 32: 1-12.

[10] Napadow V.J., Chen Q., Wedeen V.J., Gilbert R.J. 1999. Biomechanical basis for lingual tissue deformation during swallowing: Am. J. Physiology, 40: G695-G701.

[11] Napadow V.J., Kamm R.D., Gilbert R.J. 2002. Biomechanical model of sagittal bending for the human tongue. Journal of Biomechanical Engineering, 124: 547-556.

[12] Hahn EL. 1950. Spin Echoes. Phy. Rev, 80: 580-594

[13] Stejskal, E.O. 1965. Use of spin echoes in a pulsed magnetic field gradient to study anisotropic, restricted diffusion and flow. Journal of Chemical Physics. 43: 3597-3603

[14] Basser P.J., Mattiello J, LeBihan D. 1994. MR diffusion tensor spectroscopy and imaging. Biophys J, 66: 259-267

[15] Basser PJ, Pierpaoli C. 1996. Microstructural and physiological features of tissues elucidated by quantitative diffusion tensor MRI. J Magn Resonance, 111: 209-211.

[16] Cory DG, Garroway AN. 1990. Measurement of translational displacement probabilities by NMR: an indicator of compartmentation. Mag Res Med, 14: 435-444.

[17] Callaghan PT. 1993. *Principals of nuclear magnetic resonance microscopy*. Oxford Press, Great Britain.

[18] Schaafsma TJ, Van As H, Palstra WD, Snaar JE, de Jager PA. 1992. Quantitative measurement and imaging of transport processes in plants and porous media by 1H NMR. Magn Reson Imaging. 10(5):827-36.

[19] Xia Y, Callaghan PT. 1992. "One-shot" velocity microscopy: NMR imaging of motion using a single phase-encoding step. Magn Reson Med. 23(1):138-53.

[20] Gilbert RJ, Daftary S, Reese G, Weisskoff RM, Wedeen VJ. 1998. Determination of lingual myoarchitecture in whole tissue by NMR imaging of anisotropic water diffusion. Am. J. Physiol., 175: G363-369.

[21] Wedeen VJ, Reese TG, Napadow VJ, Gilbert RJ. 2001, Demonstration of primary and secondary fiber architecture of the bovine tongue by diffusion tensor magnetic resonance imaging. Biophys. J, 80: 1024-1028.

[22] Napadow VJ, Chen Q, Mai V, So PTC, Gilbert RJ. Quantitative analysis of three-dimensionally resolved fiber architecture in heterogeneous skeletal muscle tissue using NMR and optical imaging methods. Biophys. J., 80: 2968-2975, 2001.

[23] Garrido L, Wedeen VJ, Kwong KK, Spencer UM, Kantor HL. Anisotropy of water diffusion in the myocardium of the rat. Circ Res. 74(5): 789-93, 1994

[24] Reese TG, Weisskoff RM, Smith RN, Rosen BR, Dinsmore RE, Wedeen VJ. Imaging myocardial fiber architecture in vivo with magnetic resonance. Magn Reson Med. 34(6):786-91, 1995.

[25] Hsu EW, Muzikant AL, Matulevicius SA, Penland RC, Henriquez CS. Magnetic resonance myocardial fiber-orientation mapping with direct histological correlation. Am J Physiol. 274(5 Pt 2):H1627-34, 1998.

[26] Hsu EW, Henriquez CS. Myocardial fiber orientation mapping using reduced encoding diffusion tensor imaging. J Cardiovasc Magn Reson. 3(4):339-47,2001.

[27] Panin VY, Zeng GL, Defrise M, Gullberg GT. Diffusion tensor MR imaging of principal directions: a tensor tomography approach. Phys Med Biol. 47(15):2737-57, 2002.

[28] Tseng WY, Wedeen VJ, Reese TG, Smith RN, Halpern EF. Diffusion tensor MRI of myocardial fibers and sheets: correspondence with visible cut-face texture. J Magn Reson Imaging. 17(1): 31-42, 2003.

[29] Pierpaoli C, Jezzard P, Basser PJ, Barnett A, Di Chiro G. Diffusion tensor MR imaging of the human brain.
Radiology. 201(3):637-48, 1996.

[30] Wiegell MR, Larsson HB, Wedeen VJ. Fiber crossing in human brain depicted with diffusion tensor MR imaging. Radiology. 217(3):897-903, 2000.

[31] Tuch DS, Wedeen VJ, Dale AM, George JS, Belliveau JW. Conductivity tensor mapping of the human brain using diffusion tensor MRI. Proc Natl Acad Sci U S A. 98(20):11697-701, 2001.

[32] Lin CP, Wedeen VJ, Chen JH, Yao C, Tseng WY. 2003. Validation of diffusion spectrum magnetic resonance imaging with manganese-enhanced rat optic tracts and ex vivo phantoms. Neuroimage. 19(3):482-95.

[33] Tuch DS, Reese TG, Wiegell MR, Wedeen VJ. 2003. Diffusion MRI of complex neural architecture. Neuron.4;40(5):885-95.

[34] Lin CP, Wedeen VJ, Chen JH, Yao C, Tseng WY. 2003. Validation of diffusion spectrum magnetic resonance imaging with manganese-enhanced rat optic tracts and ex vivo phantoms. Neuroimage. 19(3):482-95.

[35] Cory DG, Garroway AN. 1990. Measurement of translational displacement probabilities by NMR: an indicator of compartmentation. Mag Res Med, 14: 435-444.

[36] Callaghan P.T. 1993. *Principals of nuclear magnetic resonance microscopy.* Oxford Press, Great Britain.

[37] Schaafsma T.J., Van A.H., Palstra W.D., Snaar J.E., de Jager P.A. 1992. Quantitative measurement and imaging of transport processes in plants and porous media by 1H NMR. Magn Reson Imaging. 10(5):827-36.

[38] Xia Y, Callaghan P.T. 1992. "One-shot" velocity microscopy: NMR imaging of motion using a single phase-encoding step. Magn Reson Med. 23(1):138-53.

[39] Lin CP, Wedeen VJ, Chen JH, Yao C, Tseng WY. 2003. Validation of diffusion spectrum magnetic resonance imaging with manganese-enhanced rat optic tracts and ex vivo phantoms. Neuroimage. 19(3):482-95.

[40] Stejskal, E.O. 1965. Use of spin echoes in a pulsed magnetic field gradient to study anisotropic, restricted diffusion and flow. Journal of Chemical Physics. 43: 3597-3603.

[41] Xia, Y, Whitesides, GM. 1998. Soft Lithography. Annual Review of Material Science. 28: 152-84.

[42] Xia, Y, Whitesides, GM. 1998. Soft Lithography. Annual Review of Material Science. 28: 152-84.

[43] Smith K.K., Kier W.M. 1989. Trunks, tongues, and tentacles: moving with skeletons of muscle. American Scientist 77, 29-35.

[44] Kier W.M., Smith K.K. 1985. Tongues, tentacles and trunks: The biomechanics and movement of muscular hydrostats. Zool. J. Linn. Soc., 83: 307-324

[45] Nishikawa K.C., Kier W.M., Smith K.K. 1999. Morphology and mechanics of tongue movement in the African pig-nosed Hemisus Marmoratum: A muscular hydrostatic model. J. Exp Biol., 202: 771-780.

[46] Napadow V.J., Chen Q., Wedeen V.J., Gilbert R.J. 1999. Intramural mechanics of the human tongue in association with physiological deformations. J. Biomechanics, 32: 1-12.

[47] Napadow V.J., Chen Q., Wedeen V.J., Gilbert R.J. 1999. Biomechanical basis for lingual tissue deformation during swallowing: Am. J. Physiology, 40: G695-G701.

[48] Napadow V.J., Kamm R.D., Gilbert R.J. 2002. Biomechanical model of sagittal bending for the human tongue. Journal of Biomechanical Engineering, 124: 547-556.

[49] Gilbert RJ, Daftary S, Reese G, Weisskoff RM, Wedeen VJ. 1998. Determination of lingual myoarchitecture in whole tissue by NMR imaging of anisotropic water diffusion. Am. J. Physiol., 175: G363-369.

[50] Wedeen VJ, Reese TG, Napadow VJ, Gilbert RJ. 2001, Demonstration of primary and secondary fiber architecture of the bovine tongue by diffusion tensor magnetic resonance imaging. Biophys. J, 80: 1024-1028.

[51] Napadow VJ, Chen Q, Mai V, So PTC, Gilbert RJ. Quantitative analysis of three-dimensionally resolved fiber architecture in heterogeneous skeletal muscle tissue using NMR and optical imaging methods. Biophys. J., 80: 2968-2975, 2001.

[52] Callaghan PT. 1993. *Principals of nuclear magnetic resonance microscopy.* Oxford Press, Great Britain.